

Thermal characteristics of quantum-cascade lasers by micro-probe optical spectroscopy

V. Spagnolo, G. Scamarcio, D. Marano, M. Troccoli, F. Capasso, C. Gmachl, A.M. Sergent, A.L. Hutchinson, D.L. Sivco, A.Y. Cho, H. Page, C. Becker and C. Sirtori

Abstract: The facet temperature profile and the thermal resistance of operating quantum-cascade lasers (QCLs) have been assessed using a microprobe band-to-band photoluminescence technique. Substrate-side and epilayer-side-mounted QCLs based on GaInAs/AlInAs/InP and GaAs/AlGaAs material systems have been compared. The dependence of the thermal resistance on the CW or pulsed injection conditions and its correlation with the output power have been studied. These results were used as inputs for a two-dimensional heat-diffusion model which gives the heat fluxes and the thermal conductivity of the active regions, in order to design QCLs with improved thermal properties.

1 Introduction

Quantum-cascade lasers (QCLs) are based on transitions between quantised states in GaInAs/AlInAs and GaAs/AlGaAs multiple-quantum-well structures [1, 2]. Laser emission has been reported in a wide range of mid-infrared wavelengths (3.5–24 μm) [1, 2]. Laser action in the terahertz range (67–80 μm) has been also demonstrated [3–5]. Excellent performance in terms of peak power (> 2 W) and maximum operating temperature (~ 470 K) has been achieved in the pulsed mode [6–8]. Continuous wave (CW) operation up to 320 K has been demonstrated for a buried GaInAs/AlInAs/InP (InP-based) QCL [9]. The highest operating temperature in a CW for GaAs/AlGaAs (GaAs-based) QCLs is 135 K [10]. On the other hand, the lifetime for CW operation at room temperature is much lower than that of quantum-well diode lasers. This is due to the high electrical power needed to achieve the laser threshold. The cavity losses in the mid-IR (10–30 cm^{-1}) lead to threshold currents in the kA/cm^2 range. The cascading scheme inherently requires applied threshold voltages of the order of 10 V. Moreover, the device thermal resistance is strongly increased by the ternary alloy nature of employed materials, the presence of a large number of interfaces and the associated phonon interference effects [11, 12]. These characteristics lead to the temperature of the active material being much greater than the heatsink. Thus,

the attainment of CW operation in a wider range of wavelengths and the enhancement of the maximum operating temperature requires a deeper knowledge of the key physical phenomena controlling thermal dissipation in QCLs.

In this paper, we present our recent results on the determination of the local lattice temperature and the thermal resistance in CW and pulsed operating QCLs, both in InP- and GaAs- based structures. We used a microprobe spectroscopy technique based on the analysis of the thermal induced shift of band-to-band photoluminescence (PL), similar to that already successfully used for conventional diode lasers [13]. We have compared substrate-side and epilayer-side mounted devices with identical epilayer structures. By using a heat dissipation model, we have estimated the heat flow configurations and the active region thermal conductivity. In conventional diode lasers, the facet temperature can be significantly higher than that in the device core because of nonradiative surface recombination processes. This effect is absent in QCLs, since they are unipolar devices and the emitted photon energies are well below those of recombination processes. Thus, we can use the facet temperature as a close estimate of the internal device temperature.

2 Investigated samples

2.1 InP-based QCLs

The GaInAs/AlInAs structure consists of three-well QCLs designed for emission at 8 μm [14]. The active region is composed of a ~ 0.53 - μm -thick stack of twelve active regions with interleaved injector regions sandwiched between two 0.5- μm -thick $\text{Ga}_{0.47}\text{In}_{0.53}\text{As}$ waveguide core layers. The top cladding layer is formed by an inner 2.5 μm thick $\text{Al}_{0.48}\text{In}_{0.52}\text{As}$ layer doped to $n = 1 - 2 \times 10^{17} \text{ cm}^{-3}$ and an outer 0.5- μm -thick $\text{Ga}_{0.47}\text{In}_{0.53}\text{As}$ layer heavily doped to $n = 5 \times 10^{18} \text{ cm}^{-3}$ for plasmon-enhanced confinement. The InP-substrate, doped to $n = 2 \times 10^{17} \text{ cm}^{-3}$, acts as a lower waveguide cladding layer. The devices were processed into 2.5-mm-long, 11- μm -wide, deep-etched

© IEE, 2003

IEE Proceedings online no. 20030610

doi: 10.1049/ip-opt:20030610

Paper first received 17th October 2002 and in revised form 2nd April 2003

V. Spagnolo, G. Scamarcio and D. Marano are with INFM, Dipartimento Interateneo di Fisica di Bari, Via Amendola 173, 70126 Bari, Italy

M. Troccoli, F. Capasso, C. Gmachl, A.M. Sergent, A.L. Hutchinson, D.L. Sivco and A.Y. Cho are with Bell Laboratories, Lucent Technologies, 600 Mountain Avenue, Murray Hill, NJ 07974

H. Page, C. Becker and C. Sirtori are with Thomson-CSF, Laboratoire Central de Recherches, 91404 Orsay, France

ridge waveguides and then mounted either substrate-side or epilayer-side onto copper holders using indium solder.

2.2 GaAs-based QCLs

The GaAs/Al_{0.33}Ga_{0.67}As structure [13] was grown on a GaAs substrate doped to $n = 2 - 3 \times 10^{18} \text{ cm}^{-3}$. The active layer consists of a 1.5- μm -thick stack of 36 three-well active regions designed for emission at 9.4 μm , and is sandwiched between two 3.5- μm -thick GaAs layers n-doped to $8 \times 10^{16} \text{ cm}^{-3}$ and two 1- μm -thick GaAs plasmon cladding layers heavily n-doped to $5 \times 10^{18} \text{ cm}^{-3}$. Ridge waveguides 1-mm long and 25- μm wide are defined using photolithographic techniques and reactive ion etching. Lateral trenches are filled with polymer to planarise the device which are then mounted either substrate-side or epilayer-side onto copper holders using indium solder.

3 Experimental technique and results

The PL signal was obtained by focusing the 476.2-nm line of a Kr⁺ laser, working in CW mode, directly onto the QCL front facet down to a spot of $\sim 1\text{-}\mu\text{m}$ diameter by using an $80 \times$ long-working-distance microscope objective lens. Laser-induced heating of the samples was avoided keeping the incident power density $< 10^4 \text{ W/cm}^2$. The devices were mounted into a helium-flow micro-cryostat and kept at a fixed heatsink temperature controlled with a calibrated Si-diode mounted close to the device. The sample position was controlled by a two-dimensional piezoelectric translation stage with 0.1- μm spatial resolution. The PL signal was dispersed using a 0.64 m monochromator and detected with a Si charge coupled device (CCD) cooled to 140 K, with a long-wavelength cut-off of at $\sim 1\text{ }\mu\text{m}$ or with a liquid-nitrogen-cooled GaInAs diode array detector, which extended our detection down to 1.6 μm , allowing the measurement of GaInAs-related emission, not accessible using Si CCDs.

Figure 1 shows representative PL spectra of different regions of an InP-based QCL front facet with the device off. The two bands at $\sim 0.82 \text{ eV}$ are related to the Ga_{0.47}In_{0.53}As waveguide core layers. The two layers should be nominally identical, the small energy difference between the related PL signals being probably due to a slight variation in the layers' doping and/or chemical composition. The PL spectrum of

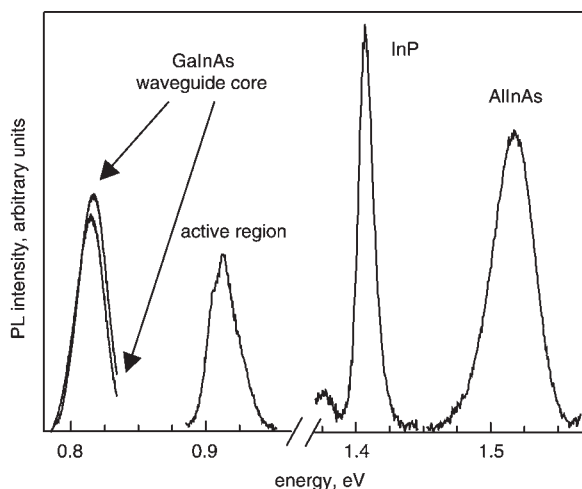


Fig. 1 Characteristic micro-probe photoluminescence spectra taken from InP-based QC laser front facet obtained with device off, at heatsink temperature of 30 K

The main peaks are labelled according to the layers from which they originate

the active region falls in energy at $\sim 0.92 \text{ eV}$. This signal is also due to Ga_{0.47}In_{0.53}As – related emission; the blue-shift observed with respect to the bulk-like Ga_{0.47}In_{0.53}As PL of the waveguide core layers is due to the quantum-confinement effect on the optical transition in the narrow Ga_{0.47}In_{0.53}As quantum well which is the active region. The PL signals coming from the InP and AlInAs cladding layers fall, respectively, at 1.42 and 1.54 eV.

A similar situation also occurs for the GaAs-based QCLs. Both the quantum confinement effect in the active region and the different doping levels of the plasmon, claddings and buffer layers allow the observation of distinct PL signals.

The shift of the PL spectra can be used as a thermometric property. In Fig. 2 are shown two series of PL spectra measured at device off in the InP (Fig. 2a) and AlInAs (Fig. 2b) cladding regions of an InP-based QCL, as a function of the heatsink temperature T_H . The PL peak energy red-shifts at increasing T_H . Thus by probing the device at zero-current while varying T_H we have determined the PL peak position as a function of the lattice temperature, thereby obtaining calibration curves for the different regions of the devices. The calibration curves obtained for the InP-based QCLs are shown in Fig. 3. Similar calibration curves have been also obtained for the different layers of the GaAs-based QCLs. We found a good agreement with known band-gap temperature dependences [15]. The rather strong temperature dependence at temperatures above 70 K ($dE_p/dT \sim 0.15 \text{ meV/K}$ in the worst case) allows

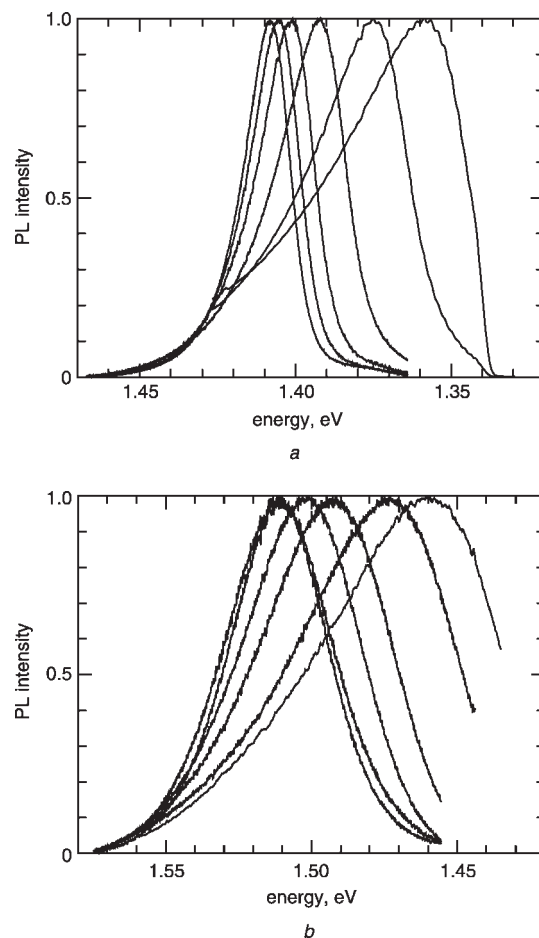


Fig. 2 Normalised photoluminescence spectra taken for the InP (a) and AlInAs (b) cladding regions of an InP-based QCL obtained at device off as a function of the heat sink temperature

In both panels the photoluminescence spectra were taken at heat sink temperatures of 85, 100, 120, 150, 210 and 270 K

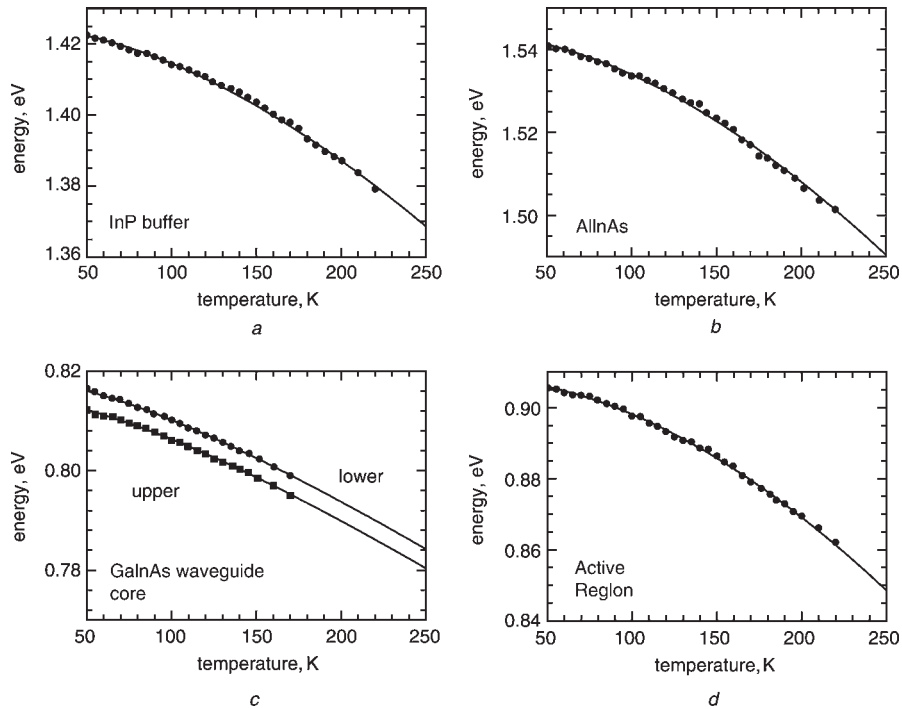


Fig. 3 Temperature dependence (symbols) of the InP substrate (a), the AlInAs top cladding layer (b), the upper (closer to the top of the ridge) and lower GaInAs waveguide core (c) and the active region (d) photoluminescence peak energy E_p , obtained varying the heat sink temperature T_H at zero-current for an InP-based QCL

E_p values were accurately determined by fitting a second-order polynomial to the PL spectrum in a 20 meV range around the peak. The continuous lines are obtained with the empirical relation $E_p(T) = E_p(0) - \alpha T^2 / (\beta + T)$, which accurately reproduces the band gap shrinkage with temperature. The lack of data above 170 K in c is related to the long wavelength cut-off (1.6 μm) of the InGaAs array detector

a temperature resolution ≤ 0.5 K. The local temperature of the laser facet is extracted by comparing the shift of the PL peak with the calibration curves for the different layers of the QCLs. In the case of PL emitted from quantum-well active regions, electric field effects have to be carefully taken into account. Comparison with self-consistent band structure calculations shows that the PL emission is dominated by two transitions between confined levels in the active layer. Figure 4 shows three PL spectra taken from

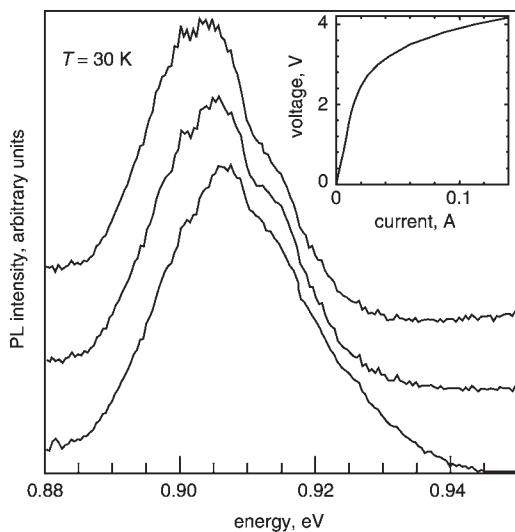


Fig. 4 Active region photoluminescence spectra taken at different applied voltages at heat sink temperature 30 K for InP-based QCL

The spectra have been taken from left to right at an applied voltage of 2 V, 1 V and with the device off, respectively. The inset shows the I-V characteristics

the active region of an InP-based QCL at different applied voltages. The red-shift of the PL peak position at increasing voltages (0–2 V) is clearly visible and cannot be ascribed to thermal heating of the device. At 2 V the corresponding electrical power is as low as 40 mW (see inset of Fig. 4) and cannot lead to any detectable heating effect on the device. In order to also use the calibration curve for quantum-well active regions, we have to determine the influence of the applied electric field, which plays a role up to threshold for current injection. Above this threshold, a small rise of the applied voltage leads to a large increase of the injected current and hence of the dissipated electrical power, whereas the electric field remains approximately constant.

Figure 5 shows the peak position of the PL arising from the active region as a function of the electrical power for an InP-based QCL. The abrupt red-shift at low dissipated power cannot be due to heating effects, and is clearly induced by the applied electric field. In the range of

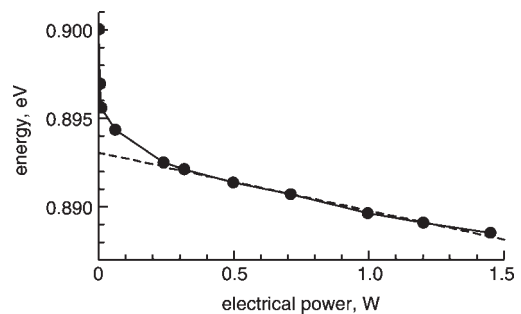


Fig. 5 Active-region photoluminescence peak energy as a function of electrical power for substrate-side-mounted InP-based QCL

The heatsink temperatures were fixed for all measurements at 80 K

electrical power ≤ 1.5 W, the thermal conductivity and hence the device thermal resistance remain approximately constant, since a temperature increase ≤ 15 K is expected. This implies that the active region temperature linearly increases with the electrical power. Further, in a small temperature range above 100 K, the active region PL peak position decreases linearly with the lattice temperature (see Fig. 3d) and consequently with the electrical power. Thus, we can extrapolate our data (see dashed line in Fig. 5) to determine the red-shift of the PL peak induced by the electric field up to the threshold for current injection, which is given by the difference between the PL peak position at device off (0.900 eV) and the intercept between the dashed line and the left vertical axis (0.893 eV). Accordingly, the calibration curve has to be scaled down by 7 meV.

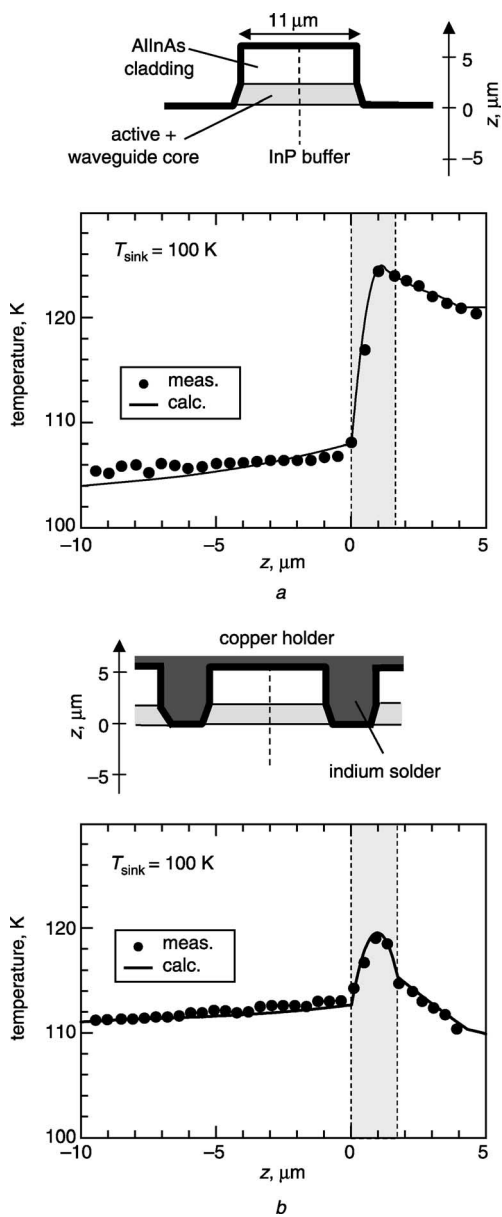


Fig. 6 Schematics of InP-based QC laser facets for substrate-side and epilayer-side mounted devices, and their corresponding measured and calculated facet temperature profiles at heat-sink temperatures of 100 K

The dashed lines indicate the locations investigated by micro-probe photoluminescence; the origin of the z-axis corresponds to the interface between the waveguide core and the InP substrate; and positive values indicate the direction towards the AllnAs cladding layers
a Substrate-side mounted
b Epilayer-side mounted

Figures 6 and 7 show the schematics of laser facets for substrate-side and epilayer-side mountings of InP-based and GaAs-based devices. Two sets of temperature profiles were obtained along the centre axis of the laser facet at $T_H = 100$ K. A CW electrical power of 3.2 W is dissipated into the InP-based laser, whereas the GaAs-based device was operated in a pulsed mode at 1 MHz with a mean electrical power of 2 W and a pulse width of 100 ns.

In spite of the different operating conditions, a few similarities appear in the experimental trends of Figs. 6 and 7. The lattice temperature in the active region of the substrate-side-mounted devices is higher than the epilayer-side ones. A stronger thermal gradient is sustained along the active region in the substrate-side-mounted devices and most of the heat flows towards the cladding layer close to the

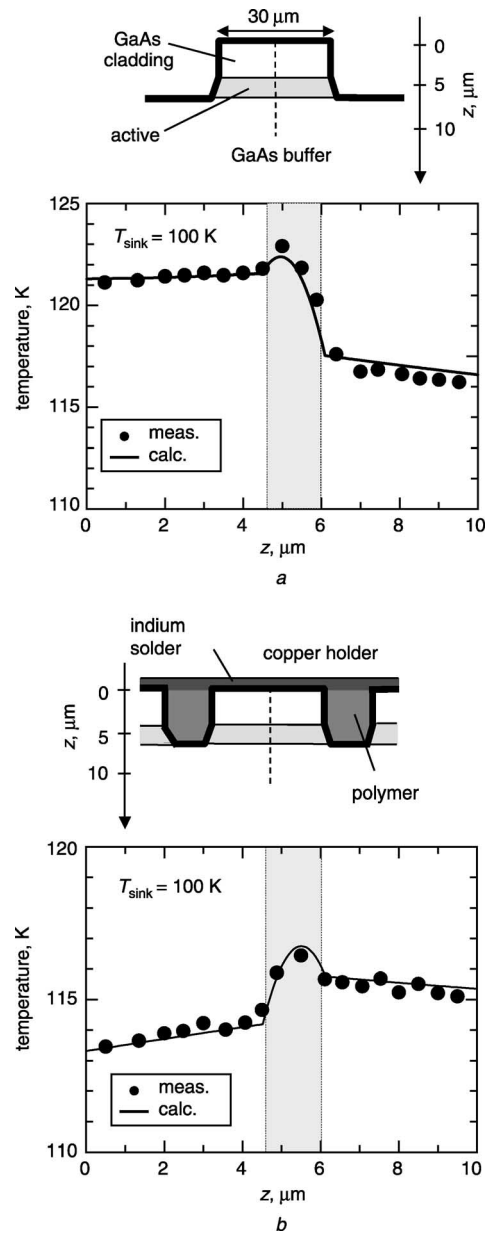


Fig. 7 Schematics of QC laser facets for substrate-side and epilayer-side mounted GaAs-based devices and their corresponding measured and calculated facet temperature profiles at heat-sink temperatures of 100 K

The dashed lines indicate the locations investigated by micro-probe photoluminescence; the origin of the z-axis corresponds to the interface between the plasmon guide and the contact layer; and positive values indicate the direction towards the active region
a Substrate-side mounted
b Epilayer-side mounted

substrate, due to the inefficient thermal link between the top of the ridge and the heatsink. On the other hand, in the epilayer-side-mounted devices, the heat flow towards the substrate and top of the ridge is comparable, as suggested by the almost equal temperatures at the boundaries of the active region.

Excellent reproductions of the experimental data have been obtained using two-dimensional models of heat dissipation (see solid curves in Figs. 6 and 7). In these models we set T_H as the boundary condition, leaving the thermal conductivity in the active region as the only fitting parameter and employed appropriate values for the thermal conductivity of the different materials in the devices.

For InP-based devices (Fig. 6) we used $2.2 \text{ W}/(\text{K cm})$ for the heat conductivity of InP and $0.15 \text{ W}/(\text{K cm})$ for the heat conductivity of $\text{Ga}_{0.47}\text{In}_{0.53}\text{As}$ [15]. The heat conductivity of $\text{Al}_{0.48}\text{In}_{0.52}\text{As}$ is scaled by a factor 1.25 with respect to that of $\text{Ga}_{0.47}\text{In}_{0.53}\text{As}$, based on the known heat conductivity values of GaAs, AlAs, InAs. The values $0.1 \text{ W K}^{-1} \text{ cm}^{-1}$, $0.87 \text{ W K}^{-1} \text{ cm}^{-1}$, $3.2 \text{ W K}^{-1} \text{ cm}^{-1}$ and $6.5 \text{ W K}^{-1} \text{ cm}^{-1}$ were used for the heat conductivity of the oxide layer, the contact layer, indium solder and copper, respectively. For GaAs-based devices (Fig. 7). Values of $1.65 \text{ W K}^{-1} \text{ cm}^{-1}$, $0.1 \text{ W K}^{-1} \text{ cm}^{-1}$, $0.87 \text{ W K}^{-1} \text{ cm}^{-1}$, $3.2 \text{ W K}^{-1} \text{ cm}^{-1}$, $0.4 \text{ W K}^{-1} \text{ cm}^{-1}$ and $6.5 \text{ W K}^{-1} \text{ cm}^{-1}$ were used for the heat conductivity of the bulk GaAs [16], oxide layer, contact layer, indium solder, polymer and copper, respectively.

In Figs. 8 and 9 the two heat flux configurations estimated from the fit of the experimental data of Figs. 6a and 6b are shown. For the substrate-side device 85% of the total heat escaping from the active region flows through the interface between the lower waveguide core layer and the InP substrate and the remaining 15% flows through the interface between the upper waveguide core layer and the AlInAs top cladding layer or laterally into the gold layer and eventually flows back into the InP substrate through the contact layer. Our calculations show that the total heat extraction through the interface between the upper waveguide core layer and the AlInAs top cladding layer is greatly enhanced (43%) in the epilayer-side-mounted device. Nevertheless, the heat

flowing towards the substrate through the interface between the lower waveguide core layer and the InP substrate, before reaching the heatsink through the contact layer and lateral channels, is still the largest one (57%) due to the higher thermal conductivity of InP. An analogous trend is observed at higher T_H .

Similar heat-flux distributions are also observed for GaAs-based QCLs. In particular, the analysis of the temperature profile of Fig. 7b gives comparable heat fluxes towards the upper cladding and towards the substrate (55% and 45%, respectively) in the epilayer-side-mounted device. In the substrate-side-mounted device (see Fig. 7a) most of the heat is dissipated through the GaAs substrate and only $\sim 27\%$ of the total heat flows towards the top of the ridge before reaching the heatsink through the contact layers and the lateral channels.

An important outcome of our analysis is the estimate of active region thermal conductivity and its temperature dependence. This information cannot be obtained by independent means in a complex multilayered structure such as ours. To our knowledge, no data on the thermal conductivities of GaInAs/AlInAs, or GaAs/AlGaAs heterostructures has been reported so far, and the use of bulk values is a quite rough approximation. In fact, due to the presence of interfaces and the inherent phonon interference effects, the thermal conductivity is expected to be considerably smaller than that of the constituent materials and has been found to be either an increasing function, as in Si/Ge [16], or a decreasing function of the temperature, as in GaAs/AlAs superlattices [17].

In Fig. 10, the active region thermal conductivity values, k_{AR} , are shown as a function of the local lattice temperature extracted from the fit of the experimental temperature profiles for the substrate-side-mounted InP-based QCL. A very good correlation between the k_{AR} values obtained for the epilayer-side and substrate-side devices at equivalent active region temperatures has been observed. As expected, k_{AR} is considerably smaller than the thermal conductivity of the constituent materials GaInAs and AlInAs, and is an increasing function of the temperature, particularly steep

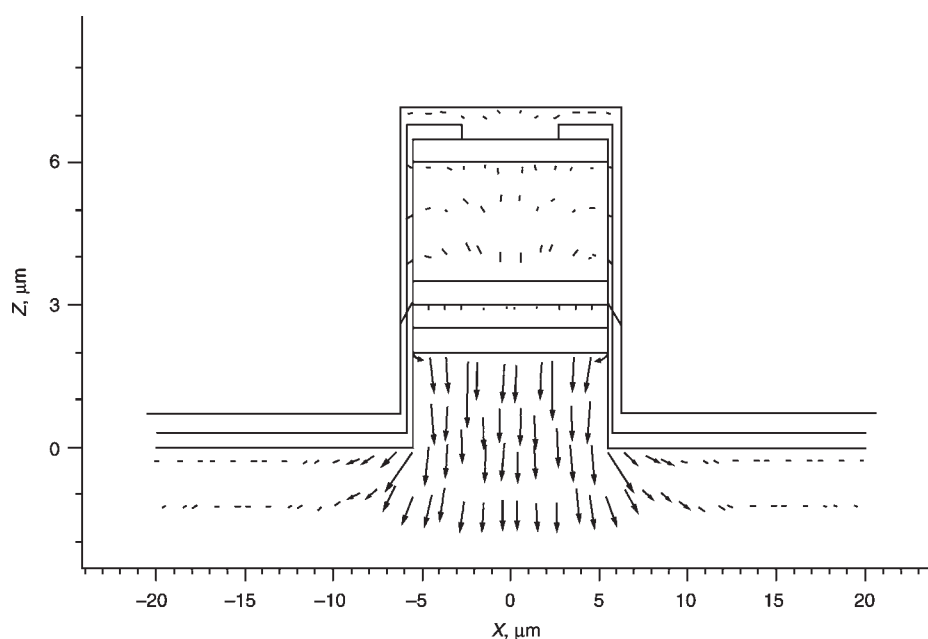


Fig. 8 Heat-flux configuration for InP-based substrate-side-mounted QCL extracted from the fit of the experimental data of Fig. 6a using the two-dimensional model of heat dissipation

The length of the vectors is proportional to the heat flux

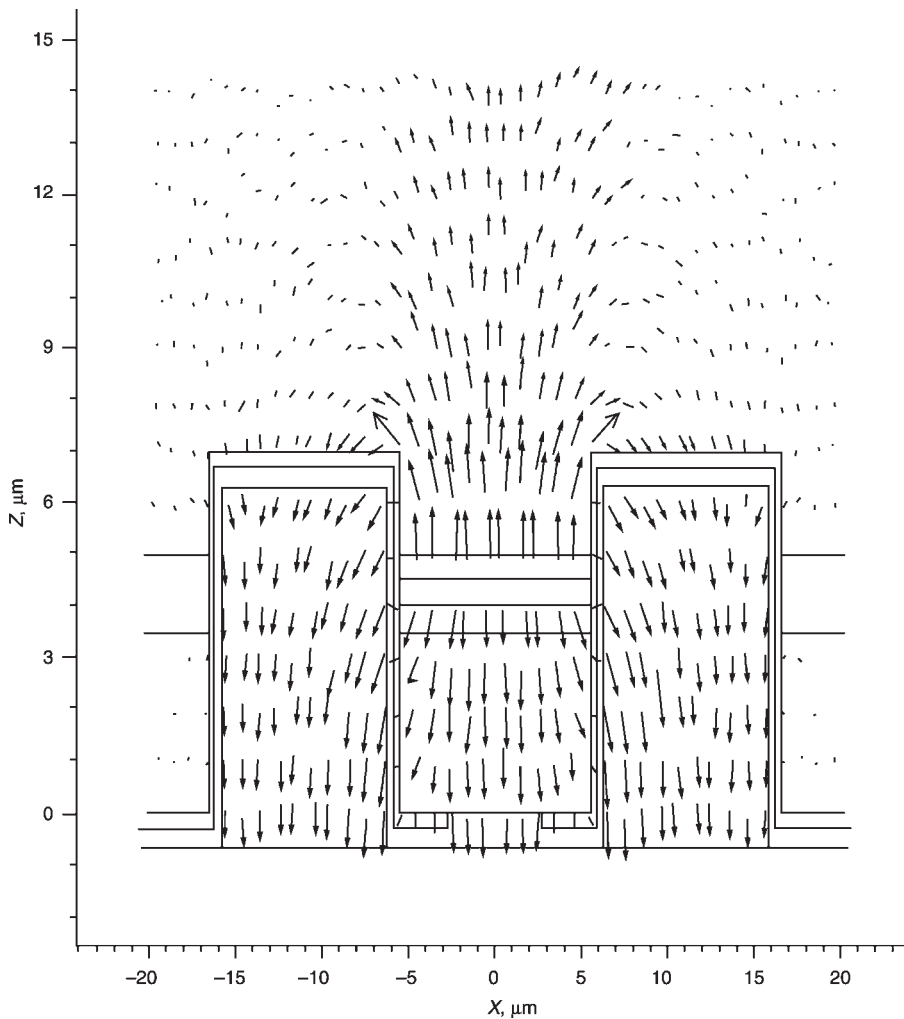


Fig. 9 Heat-flux configuration for the InP-based epilayer-side-mounted laser extracted from the fit of the experimental data of Fig. 6b using the two-dimensional model of heat dissipation

The length of the vectors is proportional to the heat flux

below 150 K. Unfortunately, existing theories do not fully explain the thermal conductivity temperature dependence even in the prototype GaAs/AlAs system [18]. A value of k_{AR} smaller than that of the constituent materials has also been found for the GaAs-based QCLs. At $T_H = 90$ K, $k_{AR} = (5.5 \pm 0.5)10^{-2}$ W/(K cm); an order of magnitude lower than that of GaAs and AlGaAs [11].

The dissimilarity in the heat-flow configurations between substrate-side and epilayer-side mounted lasers leads to an

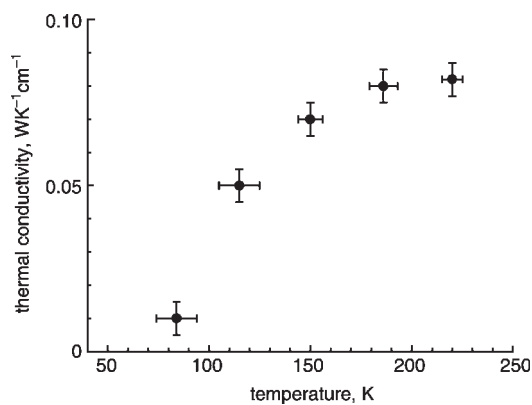


Fig. 10 Thermal conductivity of the active region of InP-based QC lasers extracted by fitting the two-dimensional model of heat diffusion to experimental temperature profiles obtained at different heatsink temperatures, 80 K–190 K

overall difference between the thermal resistances of the two devices. This quantity can be obtained from the data in Figs. 11 and 12, showing the active-region temperature as a function of the mean injected power for the InP-based and

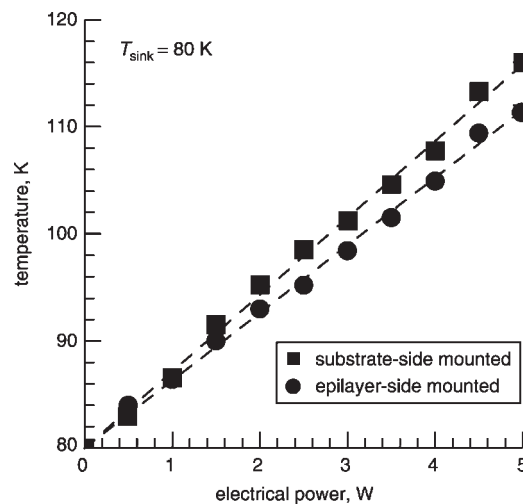


Fig. 11 Active region temperature as a function of the CW dissipated electrical power measured at heatsink temperature 80 K for InP-based QCLs

The lines are linear fits to the data and their slopes are the thermal resistances

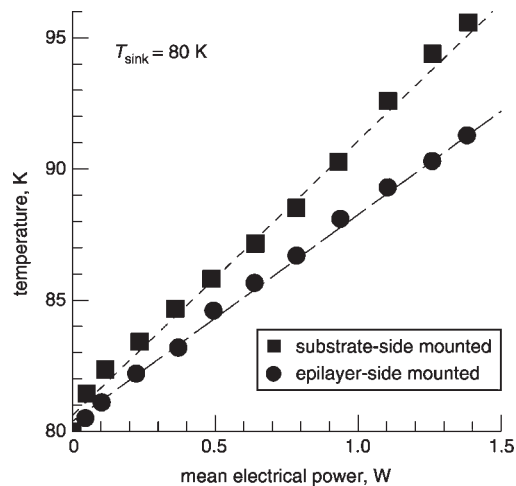


Fig. 12 Active-region temperature as a function of the electrical mean power measured at $f = 1\text{ MHz}$ and pulse width $\Delta t = 100\text{ ns}$ for GaAs-based QCLs

The lines are linear fits to the data and their slopes are the thermal resistances

GaAs-based devices, respectively. For the substrate-side-mounted InP-based devices we determined a thermal resistance $R = 7.1\text{ K/W}$ (see Fig. 11) at $T_H = 80\text{ K}$. Mounting the devices epilayer-side causes a 10% reduction of the devices thermal resistance ($R = 6.3\text{ K/W}$). This decrease leads to a performance improvement in terms of operating temperature. In fact, the maximum operating temperature of the epilayer-side mounted device (170 K) is 30 K higher than the substrate-side-mounted one.

The results of Fig. 12, obtained for GaAs-based QCLs operating in a pulsed mode show a $\sim 30\%$ reduction of R for the epilayer-side-mounted device. The pulse width was $\Delta t = 100\text{ ns}$, the repetition rate $f = 1\text{ MHz}$ and $T_H = 80\text{ K}$. The two different slopes in Fig. 12 correspond to $R = 11.2\text{ K/W}$ for the substrate-side and $R = 7.8\text{ K/W}$ for the epilayer-side-mounted lasers. In the latter, we also found that at $\Delta t = 200\text{ ns}$, $f = 1\text{ MHz}$ the thermal resistance increases to $R = 9.5\text{ K/W}$. This 10% increase is a self-heating effect, explained by the larger temperatures reached during longer pulses, which in turn cause a decrease of the thermal conductivities [17, 18].

In order to further investigate the self-heating effect, we measured the active-region mean temperature for the epilayer-side-mounted QCL at different repetition rates, keeping the pulse width fixed at $\Delta t = 100\text{ ns}$, $T_H = 80\text{ K}$, the applied voltage at $V = 7\text{ V}$ and the injected current at $I = 2\text{ A}$. The results are shown in Fig. 13a. Since the electrical power linearly increases with the repetition rate, a constant thermal resistance should lead to a linear increase of the active-region temperature. On the other hand, deviation from linearity becomes evident for $f > 300\text{ kHz}$ and corresponds to an increase of R with the repetition rate. These findings are consistent with the notion that the excess thermal energy is transferred from the semiconductor chip to the heatsink in several μs and are in qualitative agreement with time-resolved heat-transport measurements in GaAs/AlGaAs diode lasers [19]. The observed low heat-dissipation rate of the device with respect to bulk materials is related to the reduction of the phonon group velocity perpendicular to the layers [20].

The enhancement of the thermal resistance leads to performance deterioration at higher repetition rates, as confirmed by the data shown in Figs. 13b and c, where the average and peak output power are displayed as a function

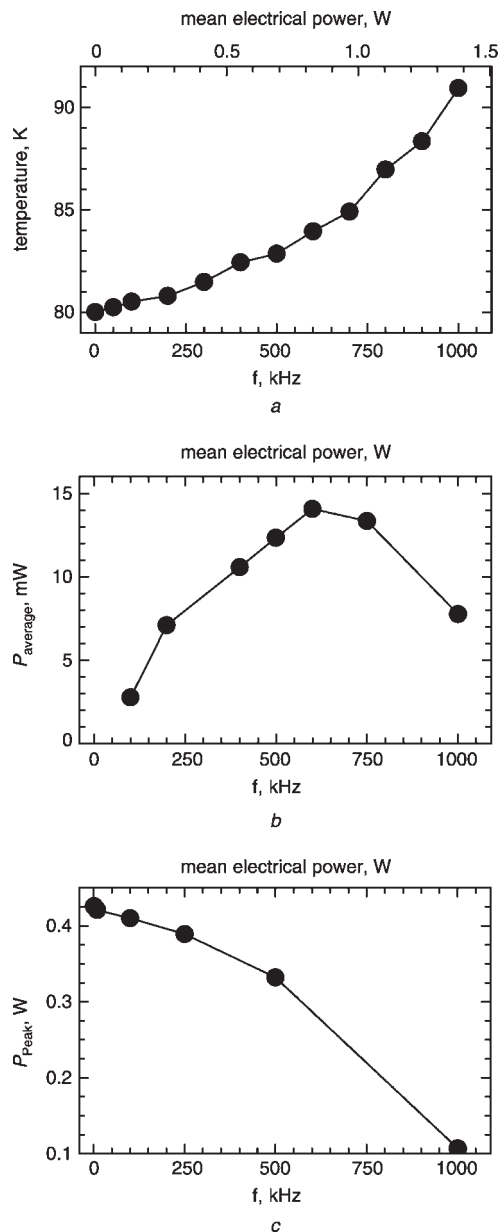


Fig. 13 Active-region mean temperature, average output power and peak power as a function of repetition rate or injected power, measured for GaAs-based epilayer-side mounted QC laser

The laser output from the front facet was collected with a $f/0.8$ optical system, and the collection efficiency was estimated to be $\eta = 0.5$

a Active-region mean temperature

b Average output power

c Peak power

of the repetition rate frequency, obtained under the same conditions as Fig. 13a. The average power (Fig. 13b) reaches a maximum of 14 mW at a repetition rate of 600 kHz and then decreases at higher frequencies, whereas the peak output power, rather than remaining constant, shows a decrease at increasing repetition rates, which becomes more intense at higher frequencies (above 250 kHz).

4 Conclusions

Using a PL microprobe technique, we have measured the facet temperatures and the thermal resistance of substrate-side and epilayer-side-mounted QCLs based on GaInAs/AlInAs/InP and GaAs/AlGaAs material systems. Thermal modelling of QCLs based on 2-D heat-diffusion theory, using our experimental data as inputs, allows

the determination of the heat-flux distribution and the active-region thermal conductivity, and gives a reliable description of the device thermal characteristics. This is crucial knowledge that will guide the development of quantum-cascade lasers in the quest for the attainment of CW operation at room temperature in the widest wavelength range.

5 Acknowledgments

This work was partly supported by INFM and MURST, cluster 26 'Materiali Innovativi', project P5WP2, and FIRB project RBAU01E8SS.

6 References

- Gmachl, C., Capasso, F., Sivco, D.L., and Cho, A.Y.: 'Recent progress in quantum-cascade lasers and applications', *Rep. Prog. Phys.*, 2001, **64**, pp. 1533–1601
- Sirtori, C., Page, H., and Becker, C.: 'GaAs-based quantum cascade lasers', *Philos. Trans. R. Soc. Lond. A, Math. Phys. Eng. Sci.*, 2001, **359**, pp. 505–522
- Kohler, R., Tredicucci, A., Beltram, F., Beere, H.E., Linfield, E.H., Davies, A.G., Ritchie, D.A., Iotti, R.C., and Rossi, F.: 'Terahertz semiconductor heterostructure laser', *Nature*, 2002, **417**, pp. 156–159
- Rochat, M., Ajili, L., Willenberg, H., Faist, J., Beere, H.E., Davies, A.G., Linfield, E.H., and Ritchie, D.: 'Low-threshold terahertz quantum-cascade lasers', *Appl. Phys. Lett.*, 2002, **81**, pp. 1381–1383
- Kohler, R., Tredicucci, A., Beltram, F., Beere, H.E., Linfield, E.H., Davies, A.G., Ritchie, D.A., Iotti, R.C., and Rossi, F.: to be published
- Scamarcio, G., Troccoli, M., Capasso, F., Hutchinson, A.L., Sivco, D.L., and Cho, A.Y.: 'High peak power (2.2 W) superlattice quantum cascade lasers', *Electron. Lett.*, 2001, **37**, pp. 295–296
- Faist, J., Hofstetter, D., Beck, M., Aellen, T., Rochat, M., and Blaser, S.: 'Bound-to-continuum and two-phonon resonance quantum-cascade lasers for high duty cycle, high-temperature operation', *IEEE J. Quantum Electron.*, 2002, **38**, pp. 533–546
- Ulbrich, N., Scarpa, G., Sigl, A., Roskopf, J., Bohm, G., Abstreiter, G., and Amann, M.C.: 'High-temperature ($T \geq 470$ K) pulsed operation of 5.5 μm quantum cascade lasers with high-reflection coating', *Electron. Lett.*, 2001, **37**, pp. 1341–1342
- Beck, M., Hofstetter, D., Aellen, T., Faist, J., Oesterle, U., Ilegems, Gini, M.E., and Melchior, H.: 'Continuous wave operation of a mid-infrared semiconductor laser at room temperature', *Science*, 2002, **295**, pp. 301–305
- Becker, C., Page, H., Calligaro, M., Ortiz, V., Garcia, M., Marcadet, X., and Sirtori, C.: 'GaAs- and GaSb- based quantum cascade lasers: the challenge of the new materials', Proc. 5th Int. Conf. on Mid-infrared optoelectronics materials and devices, Annapolis, USA, 2002, pp. 111–112
- Spagnolo, V., Troccoli, M., Scamarcio, G., Becker, C., Glastre, G., and Sirtori, C.: 'Thermal resistance and temperature characteristics of GaAs/Al_{0.33}Ga_{0.67}As quantum-cascade lasers', *Appl. Phys. Lett.*, 2001, **78**, pp. 1177–1179
- Spagnolo, V., Troccoli, M., Scamarcio, G., Gmachl, C., Capasso, F., Tredicucci, A., Sergent, A.M., Hutchinson, A.L., Sivco, D.L., and Cho, A.Y.: 'Temperature profile of GaInAs/AlInAs/InP quantum cascade laser facets measured by microprobe photoluminescence', *Appl. Phys. Lett.*, 2001, **78**, pp. 2095–2097
- Hall, D.C., Goldber, L., and Mehuys, D.: 'Technique for lateral temperature profiling in optoelectronic devices using a photoluminescence microprobe', *Appl. Phys. Lett.*, 1992, **61**, pp. 384–386
- Gmachl, C., Capasso, F., Tredicucci, A., Sivco, D.L., Kohler, R., Hutchinson, A.L., and Cho, A.Y.: 'Dependence of the device performance on the number of stages in quantum-cascade lasers', *IEEE J. Sel. Top. Quantum Electron.*, 1999, **5**, pp. 808–816
- Madelung, O., Schultz, M., and Weiss, H.: 'Landolt-Börnstein Tables, Group III' (Springer-Verlag, Berlin 1982), vol. 17a
- Lee, S.M., Cahill, D.G., and Venkatasubramanian, R.: 'Thermal conductivity of Si-Ge superlattices', *Appl. Phys. Lett.*, 1997, **70**, pp. 2957–2959
- Hall, D.C., Maris, H.G., Ruf, T., Cardona, M., Ploog, K., and Katzer, D.S.: 'Thermal-conductivity measurements of GaAs/AlAs superlattices using a picosecond optical pump-and-probe technique', *Phys. Rev. B, Condens. Matter*, 1999, **59**, pp. 8105–8113
- Chen, G.: 'Thermal conductivity and ballistic-phonon transport in the cross-plane direction of superlattices', *Phys. Rev. B, Condens. Matter*, 1998, **57**, pp. 14958–14973
- Voos, M., Lier, C., Menzel, U., Bärwolff, A., and Elsaesser, T.: 'Time-resolved emission studies of GaAs/AlGaAs laser diode arrays on different heat sinks', *J. Appl. Phys.*, 1996, **79**, pp. 1170–1172
- Tamura, S., Tanaka, Y., and Maris, H.J.: 'Phonon group velocity and thermal conduction in superlattices', *Phys. Rev. B, Condens. Matter*, 1999, **60**, pp. 2627–2630

Copyright of IEE Proceedings -- Optoelectronics is the property of IEE and its content may not be copied or emailed to multiple sites or posted to a listserv without the copyright holder's express written permission. However, users may print, download, or email articles for individual use.